# Initiating an efficient electrocatalyst for water splitting *via* valence configuration of cobalt-iron oxide

Peng Guo[a], Zhaojie Wang[a,*], Tian Zhang[a], Chen Chen[b], Yalan Chen[b], Haijun Liu[c], Minglei Hua[a], Shuxian Wei[c], Xiaoqing Lu[a,*]

[a] *School of Materials Science and Engineering, China University of Petroleum, Qingdao, 266580, People's Republic of China*
[b] *College of Chemical Engineering, China University of Petroleum, Qingdao, 266580, People's Republic of China*
[c] *College of Science, China University of Petroleum, Qingdao, 266580, People's Republic of China*

A B S T R A C T

Engineering valence state of active center in non-noble metal-based electrocatalysts is of prime importance to enhance the performance for different catalytic reactions. However, studies on optimized valence configuration with extremely high activity remains a great challenge because of scanty chemical approaches. Herein, a kind of CoFe-oxide nanocubes with tunable valence composition was rationally designed for boosting water splitting electrocatalysis by partially chemical tailoring Prussian blue analogue. The resulting $Co^{2+}$-rich CoFe-oxide nanocube ($Co^{II}$Fe-ONC) exhibited higher OER and HER catalytic performance than the well-balanced CoFe-oxide. It demanded overpotentials of only 289 mV and 284 mV to drive a current density of 50 mA cm$^{-2}$ for OER and HER in 1.0 M KOH, respectively. The DFT calculations revealed that $Co^{II}$Fe-ONC is more favorable for OER and HER since the higher capacity of water adsorption, optimized route for electrons transferring, and lower energy barrier for water dissociation by the active valance configuration.

## 1. Introduction

Increasingly serious energy crisis and environment issues have driven urgent research for clean and sustainable energy systems [1]. Electrochemical water splitting is considered as a promising approach to generate hydrogen and oxygen in large scale [2,3]. The thermal dynamically uphill of oxygen evolution reaction (OER) makes it a kinetic bottleneck as well as the high cost of noble metal catalysts (Pt-, Ru- and Ir-based materials) for both OER and hydrogen evolution reaction (HER), which promote the development of non-noble transition metal-based active catalysts with commercially viable rates [4–7]. First-row transition metals have been extensively explored as attractive candidates for HER and OER catalysis on account of their splendid performance and earth-abundance [8,9]. Decades of research have accumulated some knowledge and yield catalysts design strategies focusing on transition metal oxide according to the "volcano" relation model [10–13]. In particular, cobalt-based oxides have been considered as the most comparable water oxidation catalyst to $RuO_2$ due to their redox stability and variable valence states [14–16]. However, great limits like sluggish kinetics, poor conductivity and inactive surface/localized electron structure still existed to hamper the application [17,18].

To date, considerable efforts have been devoted to improve the atomic and electronic structures of cobalt-based oxides *via* tuning chemical component [19], constructing nanostructure with dimensional confinement [20], fabricating low-crystallinity and amorphous catalysts [21], doping with cations or anions [17,22–24], introducing vacancies/defects [25,26], creating nanointerface in hybrids [27], *etc*. Interestingly, metal organic frameworks (MOFs) composed of metal centers/clusters bridged by functional organic ligands possess comprehensive characteristics including high porosity, three dimensional structures, and compositional flexibility, which provide more opportunities to tune the mentioned atomic and electronic structures simultaneously [28]. One cheaper example is Prussian blue analogues (PBAs), which can be described as $M_x[N_y(CN)_6]_z$ (M, N = transition metals). The conventional understanding is that there are two different hosts for homogeneously distributing different metals with various M/N ratios. It endows PBA as an excellent precursor for designing multi-metal oxide electrocatalysts with redox active sites and mixed conductivity.

The composition-activity relationship has been proposed to advance their applications for HER and OER. For example, Ashwani Kumare et al. prepared NiFe-oxide nanocubes for overall water splitting from the NiFe-PBA [29]. Zhang et al. designed the $CoFe_2O_4$ thin film

supported on the Ni foam from the CoFe-PBA thin film with excellent OER performance [30]. Absolutely, diverse complex PBA nanostructures can also provide more opportunities to tune the surface area, porosity and open sites for adsorption. Hu and co-workers prepared PB hollow particles with porous shells by a controlled self-etching reaction on PB mesocrystals [31]. Lou et al. fabricated Ni-Co-mixed oxide nanocages from chemical etched Ni-Co PBA and found that the inhomogeneous surface reactivity of solid Ni-Co PBA nanocubes is crucial for the cage-like morphology [19]. Wen et al. obtained the oxygen-containing amorphous cobalt sulfide porous nanocube from the CoFe-PBA through a solvent thermal reaction with $Na_2S$ [32]. One of the more remarkable aspects is that these transition metals have different valence at different positions in PBA-derived active materials. For example, in a typical spinel $CoFe_2O_4$ bivalent ions mainly distribute in the tetrahedral space formed by divalent oxygen ions while in an inverse spinel crystal they locate at the octahedral space and the tetrahedral space. The valence states of metal-centers in active materials have a great impact on the charge distribution and electronic structure [33]. However, few researches have been well documented in the literatures and our fundamental understanding is poor due to the serious difficulty to adjust the metal valences initiated from the integrated synthesis environment. In this context, we focused on the determination of tunable valence states for advancing water splitting activities, which may lead to effective catalyst design principles.

In this study, we present a design of CoFe oxide nanocubes confined with $Co^{2+}$-rich active metal-centers to accelerate electron transfer rate for enhancing HER and OER activities in alkaline. PBA nanocubes with a chemical formula $Co_x[Fe(CN)_6]_y \cdot zH_2O$, where Co and Fe are divalent and trivalent cations, are selected as the MOF precursor. More specifically, a chemical tailoring method is applied to vary metal-centers states before obtaining valence tunable CoFe oxides. We identify a significant change of valence states in the PBA-derived active oxides and the $Co^{II}Fe$-ONC exhibits superior OER and HER performance in 1.0 M KOH to well-balanced CoFe-oxide. Density functional theory (DFT) calculations are used to explore the enhancement mechanism of valence configuration. The unprecedented electrocatalytic performance manifests the importance of valence states engineering in designing transition metal-based water splitting electrocatalysts.

## 2. Results

### 2.1. Synthesis and morphological characterization

Fig. 1a illustrates the synthesis of $Co^{II}Fe$-ONC derived from CoFe-PBA precursor according to a traditional co-precipitation method. The morphologies of the samples were tracked by transmission electron microscope (TEM) and field-emission scanning electron microscope (FESEM). As shown in Fig. 1b and c, the CoFe-PBA precursor is a typical nanocube with a uniform size of ˜260 nm. A chemical tailoring method was applied to modify the as-prepared CoFe-PBA and the intermediate labelled as $Co^{II}Fe$-PBA nanocubes with a rough surface were obtained. As observed from Fig. 1d and e, the size of $Co^{II}Fe$-PBA is about 250 nm, slightly smaller than that of CoFe-PBA. The chemical tailoring process is of prime importance for tuning valence configuration. The detailed changes in structure and composition before and after the chemical tailoring treatment were recorded by X-ray diffraction (XRD) pattern and XPS spectra in Fig. S1 and S2. The diffraction peaks of both CoFe-PBA and $Co^{II}Fe$-PBA were located between the standard data of $Co_3[Fe(CN)_6]_2 \cdot 10H_2O$ and $Co_2[Fe(CN)_6] \cdot 2H_2O$, indicating a mixture of them. As shown in Fig. S2, slight changes can be observed for Co 2p while great changes occurred for Fe 2p during the chemical tailoring. The content of Fe(III) increases obviously along with the evident blue shifts for Fe $2p_{3/2}$ and $2p_{1/2}$ peaks according to the comparison. It demonstrates that chemical tailoring may provide suitable condition for the conversion from the $^{II}Co$-NC-$Fe^{II}$ to the $^{II}Co$-NC-$Fe^{III}$.

To have better understanding of the chemical tailoring process,

CoFe-PBA was treated by the similar process in $NaH_2PO_4$ solution and water without solute to prepare S-CoFe-PBA and W-CoFe-PBA, respectively. Different from the red shift for $Co^{II}Fe$-PBA comparing with CoFe-PBA in XRD patterns, the evident blue shift for both S-CoFe-PBA and W-CoFe-PBA can be observed (Fig. S1b), indicating that $Co_2[Fe(CN)_6] \cdot 2H_2O$ is dominating in S-CoFe-PBA and W-CoFe-PBA while $Co_3[Fe(CN)_6]_2 \cdot 10H_2O$ in $Co^{II}Fe$-PBA comparing with CoFe-PBA. Furthermore, compared with more $Fe^{3+}$ in $Co^{II}Fe$-PBA in Fig. S2a, $Fe^{2+}$ increases in W-CoFe-PBA and S-CoFe-PBA along with $Fe^{3+}$ disappears from the Fe 2p spectra in Fig. S3. It indicates that $H_2O$ may facilitate the transfer from $[Fe(CN)_6]^{3-}$ to the $[Fe(CN)_6]^{4-}$ in a solvothermal method while $NH_4^+$-rich solution promotes the reverse conversion. $H_2PO_4$- is adsorbed on $Co^{II}Fe$-PBA and S-CoFe-PBA (Fig. S4), which prevents $Co^{2+}$ from being oxidized [34].

Thermogravimetric analysis (TGA) of $Co^{II}Fe$-PBA and CoFe-PBA was conducted in air and $N_2$, respectively. As shown in Fig. S5, the cyano-bridged framework can scarcely be broken in $N_2$ before 500℃ while the PBA precursors can convert into stable CoFe oxide in air at only 350℃. The final $Co^{II}Fe$-ONC were obtained by sintering $Co^{II}Fe$-PBA at 350℃ for 2 h in air. According to the SEM and TEM images in Fig. 1f–h, the size of $Co^{II}Fe$-ONC reduces to 210 nm with grooves on the rough face. Its elemental composition and dispersion of Co, Fe and O were confirmed by EDX element mapping (Fig. 1j–m). In the HRTEM image (Fig. 1i), lattice spacing of 0.478 nm can be assigned to (111) plane of inverse spinel structure, which is between those of $Co_3O_4$ (0.467 nm) and $CoFe_2O_4$ (0.485 nm) [35]. For comparison, the well-balanced CoFe-ONC derived from CoFe-PBA were prepared and characterized as shown in Fig. S6. The Co/Fe atomic ratio in both the precursors and final oxides were measured by Inductively Coupled Plasma Mass Spectrometry (ICP-MS) and listed in Table S1. There is no obvious change in Co/Fe ratio as they remain the same stoichiometry even being treated in hydrothermal reaction.

The crystal structures of the as-prepared samples were examined by XRD. As shown in Fig. 2a, the weak and broad peaks of both CoFe-ONC and $Co^{II}Fe$-ONC located between the standard peaks of $Co_3O_4$ (PDF#43-1003) and $CoFe_2O_4$ (PDF#22-1086) can be assigned to inverse spinel structure of CoFe oxides, which would endow a better OER performance than a typical spinel crystal by lengthening the O−O bond adsorbed on the surface [35]. Furthermore, the poor crystallinity is expected to expose more active sites due to crystal defects. The $N_2$ adsorption/desorption measurement was carried out to evaluate the surface area and pore features of the as-prepared catalysts. As shown in Fig. 2b, the $Co^{II}Fe$-ONC displays a type-IV $N_2$ adsorption and desorption isotherm, while the CoFe-PBA, $Co^{II}Fe$-PBA and CoFe-ONC display type-I, type-IV and type-IV isotherm, respectively (shown in Fig. S7a-c). Both the BET surface area and pore diameter distribution of $Co^{II}Fe$-ONC is similar to that of CoFe-ONC while greatly different from that of CoFe-PBA ($288.2 \, m^2 \, g^{-1}$) and $Co^{II}Fe$-PBA ($257.3 \, m^2 \, g^{-1}$). The large surface area and mesoporous structure might expose fruitful active sites and facilitate mass transport for advanced electrochemical performance even overall water splitting.

### 2.2. Valence and electronic state characterization

As the chemical tailoring process modifies the valence state of the PBA precursor, XPS were also performed to get insight into the chemical state of the final CoFe oxides. Fig. 2c displays the high resolution Co 2p spectra of $Co^{II}Fe$-ONC and CoFe-ONC, which have been found as Co $2p_{3/2}$ and $2p_{1/2}$. The peaks at 781.8 and 796.9 eV can be indicated as $Co^{2+}$, while those at 780.2 eV and 795.2 eV are $Co^{3+}$. The coexistence of $Co^{2+}/Co^{3+}$ and $Fe^{2+}/Fe^{3+}$ (Fig. S8) in both $Co^{II}Fe$-ONC and CoFe-ONC further demonstrates the inverse spinel structure. Based on the fine-scanning and well fitted results, there is an evidently blue shift for Co 2p, indicating a higher $Co^{2+}$ content in $Co^{II}Fe$-ONC. The ratio of $Co^{2+}/Co^{3+}$ increases from 0.49 in CoFe-ONC to 2.27 in $Co^{II}Fe$-ONC. Correspondingly, a higher $Fe^{3+}/Fe^{2+}$ ratio in $Co^{II}Fe$-ONC is observed
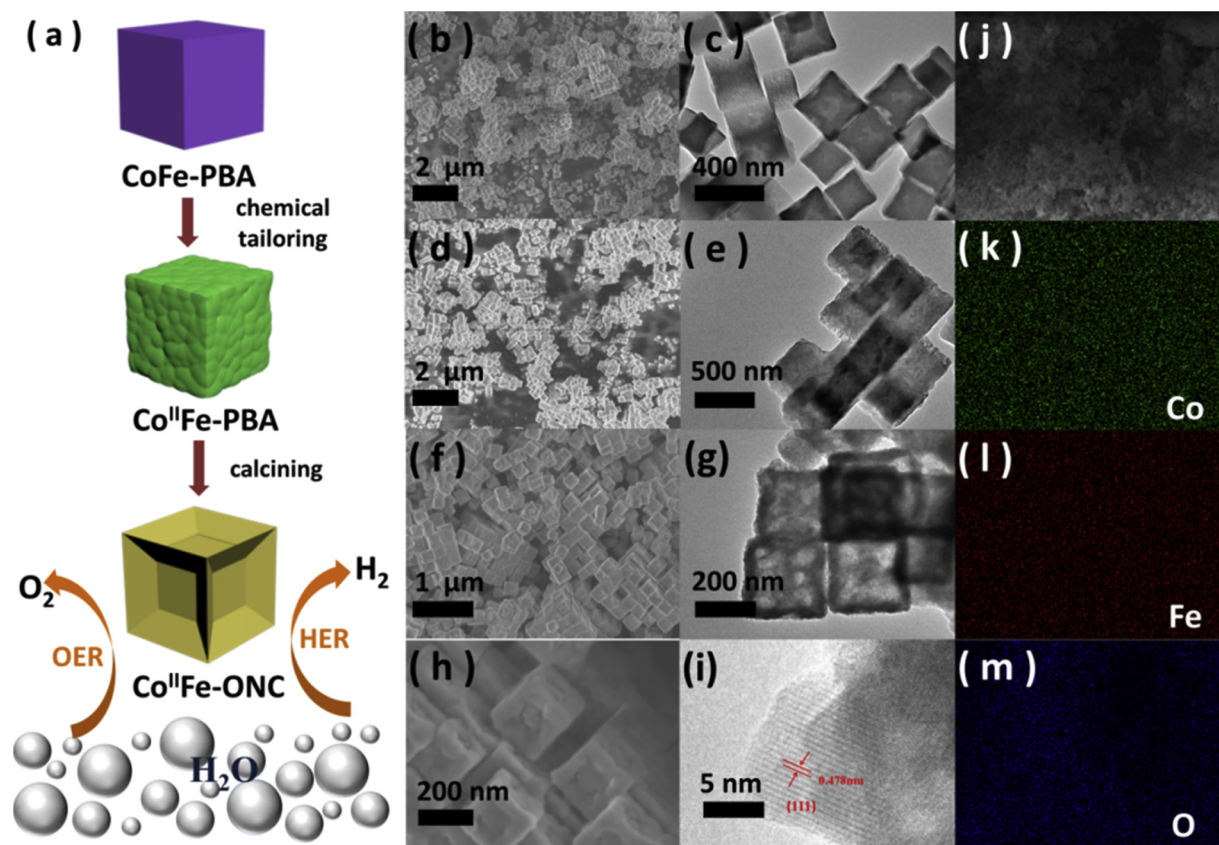
**Fig. 1.** (a) Schematic illustration of the formation of Co$^{II}$Fe-ONC electrocatalyst. (b) SEM image and (c) TEM image of CoFe-PBA. (d) SEM image and (e) TEM image of Co$^{II}$Fe-PBA. (f), (h) SEM images, (g) TEM image and (i) HRTEM image of Co$^{II}$Fe-ONC. (j) SEM image and (k~m) the corresponding element mapping of Co$^{II}$Fe-ONC.

to balance the inverse spinel structure suggesting that the $Fe^{3+}/Fe^{2+}$ may play an important role to adjust the $Co^{2+}/Co^{3+}$ through the chemical tailoring. Similarly, W-CoFe-PBA and S-CoFe-PBA were calcined in the same condition to obtain W-CoFe-ONC and S-CoFe-ONC, respectively. Calculated from the Fe 2p spectra in Fig. S9a, the similar $Fe^{3+}/Fe^{2+}$ ratio in W-CoFe-ONC (~1.00) and S-CoFe-ONC (~1.01) is achieved from the $Fe^{2+}$-rich CoFe-PBA. However, the higher $Co^{2+}/Co^{3+}$ ratio in Co$^{II}$Fe-ONC (~2.27) and S-CoFe-ONC (~1.04) than that of W-CoFe-ONC (~0.26) is achieved in Fig. S9b as well. It also demonstrates that the $H_2PO_4^-$ adsorbed on S-CoFe-ONC and Co$^{II}$Fe-ONC may prevent the $Co^{2+}$ in PBA from being oxidized.

The valence composition can be easily tuned by the chemical tailoring temperature (*e.g.* 120, 150 and 180℃). The intensity ratio of $Co^{2+}/Co^{3+}$ for Co$^{II}$Fe-ONC shows a clear increase with respect to CoFe-ONC, indicating a continuous increase in the $Co^{2+}$ content with increasing hydrothermal temperature (Fig. S10a). The comparison of O 1s spectra in Figs. 2d and S10b illustrates a higher ratio of O2/O1 in Co$^{II}$Fe-ONC (the O1 ascribes the O bound to the metals, while the O2 is formed by the low oxygen coordination defects), in accordance with the previous studies that a higher $Co^{2+}/Co^{3+}$ could be indicative of a higher oxygen vacancy density (Fig. S10b) [26,36]. The high O-vacancy improves the water adsorption during the OER and HER in the alkaline solution, which will be in favor of excellent electrocatalysts with high activity and fast kinetics [37].

### 2.3. OER properties in alkali

Electrocatalytic performance parameters extracted from the composition series show abrupt change upon adjusting valence states of cobalt. The OER performances were evaluated in 1 M KOH with a standard three-electrode setup. For comparison, initial carbon fiber paper (CFP), commercial $RuO_2$, PBA precursors and CoFe oxides with

different valence compositions were investigated. Fig. 3a presents the *iR*-corrected linear sweep voltammetry (LSV) curves. The commercial $RuO_2$ still behaves the smallest onset potential among our catalysts. Notably, it needs an overpotential of 258 mV for Co$^{II}$Fe-ONC to reach a current density of 10 mA cm$^{-2}$, which is only 15 mV higher than that of $RuO_2$. With the test current density increasing to 27 mA cm$^{-2}$, the OER performance of Co$^{II}$Fe-ONC exceeds the others *e.g.* an overpotential of 289 mV to approach 50 mA cm$^{-2}$. In sharp contrast, CoFe-ONC, Co$^{II}$Fe-PBA and CoFe-PBA shows overpotentials of 428, 311 and 425 mV to afford the current density of 50 mA cm$^{-2}$. In the practical case, the LSV polarization curves without *iR* compensation were recorded and shown in Fig. S11, illustrating the evident enhancement of OER performance from CoFe-ONC to Co$^{II}$Fe-ONC.

According to the classical analysis of OER, the Tafel plots were obtained from the Tafel equation [$\eta = $ b log(j) + a, where $\eta$ is the overpotential, j is the current density, and b is the Tafel slope] and shown in Fig. 3b. The Tafel slope of Co$^{II}$Fe-ONC is only 41.6 mV·dec$^{-1}$, which is much smaller than that of CoFe-ONC (78.4 mV·dec$^{-1}$), Co$^{II}$Fe-PBA (53.6 mV·dec$^{-1}$), CoFe-PBA (94 mV·dec$^{-1}$), and even the commercial $RuO_2$ (73.2 mV·dec$^{-1}$), implying the more favorable OER kinetics of Co$^{II}$Fe-ONC catalyst. The smaller value of Co$^{II}$Fe-ONC than that of the well-balanced samples confirms our expectation that $Co^{2+}$ is key for electrocatalysis in alkaline electrolyte. The low valence of the transition metal may facilitate electrons transferring and promote the catalytic performance according to the favorable oxygen reduction reaction (ORR) performance for the Co/CoO supported on the graphene, [38] mixed valence $CoO_x$ nanocrystals supported on N-doped carbon nanocages, [39] and the oxygen activation for the FeO/Pt [40]. As for the OER performance of Co(II)-rich catalysts, the $Co^{2+}$ as the main active sites may be the dominating electron releaser under applied bias and responsible for the formation of cobalt oxyhydroxide (CoOOH) in OER [21,41].
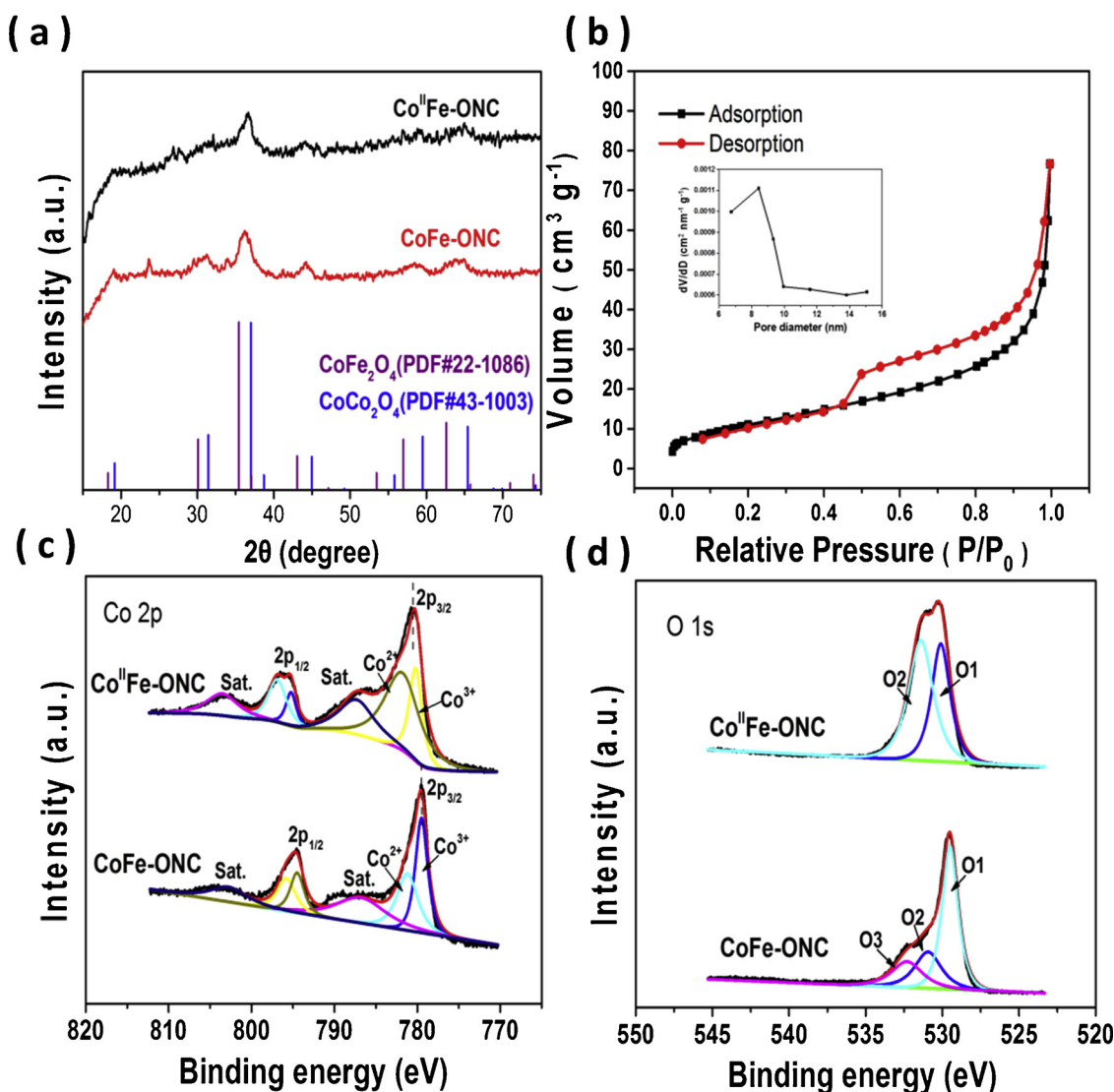
Fig. 2. (a) XRD patterns of $Co^{II}Fe$-ONC and CoFe-ONC. (b) $N_2$ adsorption and desorption isotherm of $Co^{II}Fe$-ONC. The inset is the pore size distribution isotherm of $Co^{II}Fe$-ONC. High resolution XPS spectra of (c) Co 2p and (d) O 1s for $Co^{II}Fe$-ONC and CoFe-ONC.

Fig. 3c shows the Faraday efficiency tested at a high current density of 100 mA·cm$^{-2}$, implying a high Faraday efficiency of 92% at a high current density. Loss of the Faradaic efficiency may be attributed to the side reactions and deviation at high current density. [42] To better understand the enhanced electrocatalytic activity of $Co^{II}Fe$-ONC, the electrochemical impedance spectroscopy (EIS) was taken out at an overpotential of 355 mV in 1 M KOH as depicted in Fig. 3d. According to the Nyquist plots, the $Co^{II}Fe$-ONC has the smallest charge transfer resistance ($R_{ct}$) of 1.15Ω than that of CoFe-ONC (9.79Ω), $Co^{II}Fe$-PBA (2.05Ω), and CoFe-PBA (5.62Ω), indicating a better electronic transmission and expedited Faradic process on the $Co^{II}Fe$-ONC catalyst electrode. ECSA is known to be proportional to the electrochemical double-layer capacitance ($C_{dl}$), which can be calculated by the detailed CV tests with different scan rates (Fig. S12). In Fig. 3e, the $C_{dl}$ value of $Co^{II}Fe$-ONC (63.7 m F cm$^{-2}$) is smaller than that of CoFe-PBA (67 m F cm$^{-2}$) and $Co^{II}Fe$-PBA (78.4 m F cm$^{-2}$). The high $C_{dl}$ of CoFe-PBA and $Co^{II}Fe$-PBA can be attributed to the intrinsic advantages of high porosity and 3D opening structures of PBA. However, it is three times to that of CoFe-ONC (22.6 m F·cm$^{-2}$). As illustrated in Fig. S13, when normalized to the ECSA (Table S2), $Co^{II}Fe$-ONC still displays the higher current density, indicating that the $Co^{II}Fe$-ONC after the chemical tailoring treatment is intrinsically more active.

The turnover frequency (TOF) reflects the intrinsic activity of each catalytic site, which can be calculated by the equation: TOF = jA/4Fm (details are recorded in the experiment section). The CV curves at a potential range of 1.025 V~1.625 V vs. RHE are shown in Fig. S14 and the corresponding slope plots are collected in Fig. S15. The TOF of $Co^{II}Fe$-ONC is 0.593 s$^{-1}$ (0.593 molecules of oxygen were produced per second per active site) at an overpotential of 270 mV, which is ~8 times of $Co^{II}Fe$-PBA and even much higher than those well-balanced catalysts (as shown in Fig. 3f). The long term stability test to OER is also crucial for the practical application. Fig. 3g shows the LSV curves of $Co^{II}Fe$-ONC before and after 1000 CV cycles (Fig. S16a) in a potential range of 1.505 V ~ 1.605 V vs RHE. No visible increase of overpotential from the LSV curves neither with (Fig. 3g) nor without (Fig. S16b) iR compensation proves the strong stability of $Co^{II}Fe$-ONC. In addition, the chronopotentiometric curve with multi-current steps (Fig. 3h) and the chronoamperometry curves (Fig. 3i) at a static overpotential of 0.305 V vs. RHE were tested without iR compensation, further confirming the excellent OER stability of $Co^{II}Fe$-ONC.

2.4. HER and overall water splitting properties in alkali

In addition, $Co^{II}Fe$-ONC also displayed favorable HER property in
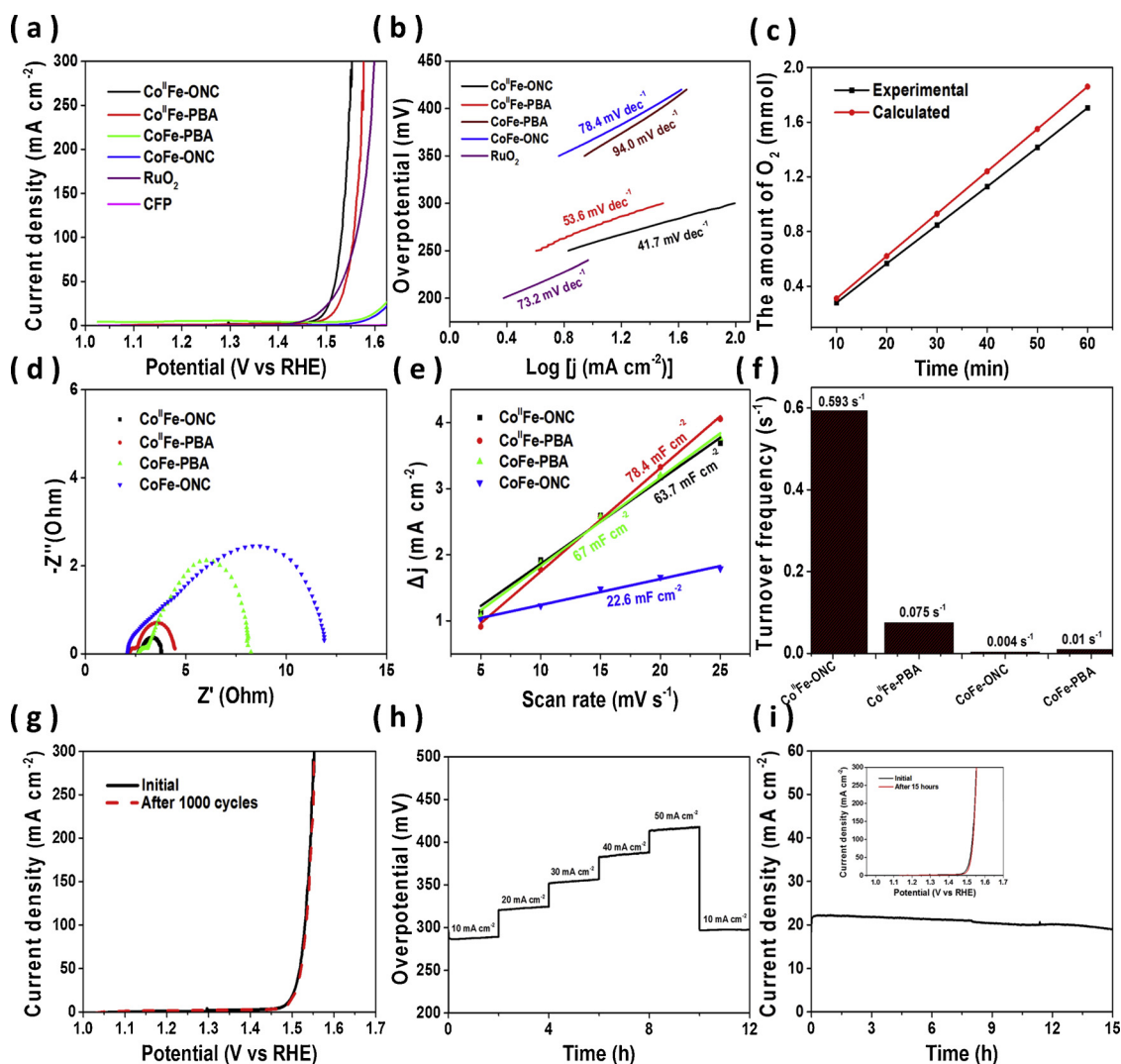
**Fig. 3.** OER performance of the as-prepared catalysts. (a) LSV curves with 95% *iR* compensation of the as-prepared catalysts, CFP and commercial RuO$_2$. (b) The corresponding Tafel plots. (c) Faradaic efficiency measurement of Co$^{II}$Fe-ONC with a current density of 100 mA cm$^{-2}$. (d) EIS Nyquist plots, (e) Capacitive current density against scan rate, and (f) TOF of the as-prepared catalysts at an overpotential of 270 mV. (g) LSV curves with 95% *iR* compensation of the Co$^{II}$Fe-ONC electrode before and after the 1000 cycles. (h) Long-term stability test of Co$^{II}$Fe-ONC at different current density steps without *iR* compensation. (i) Current versus time data on a Co$^{II}$Fe-ONC at 1.535 V for 15 h without *iR* compensation. The inset presents the corresponding LSV curves with 95% *iR* compensation before and after 15 h stability test.

1 M KOH. As shown in Fig. 4a, the Co$^{II}$Fe-ONC can reach the current density of 50 mA·cm$^{-2}$ at an overpotential of 284 mV, which is smaller than the other catalysts we prepared. The LSV curves without *iR* compensation were also shown in the Fig. S17. Similarly, after normalized to the ECSA, Co$^{II}$Fe-ONC also show higher HER activity compared to CoFe-ONC (Fig. S18). Besides, Fig. 4b demonstrates the smaller Tafel slope of Co$^{II}$Fe-ONC (75.8 mV s$^{-1}$) proceeding *via* a Volmer−Heyrovsky mechanism [43,44]. Fig. 4c shows the Faradaic efficiency of Co$^{II}$Fe-ONC for HER tested at a high current density of 100 mA cm$^{-2}$, and it reaches 91.5%. The superior HER performance of Co$^{II}$Fe-ONC to the corresponding well-balanced catalyst confirms the advance of low valance configuration of Co in HER as well. The outstanding HER stability of Co$^{II}$Fe-ONC was tested by the chronoamperometry at an overpotential of 340 mV (Fig. 4d) and the LSV curves before and after the chronoamperometry test were shown in the inset of the Fig. 4d.

Given that Co$^{II}$Fe-ONC exhibits superior catalytic activity and stability for both OER and HER, which are comparable to the results reported recently (Table S3). Specially, Co$^{II}$Fe-ONC holds great promise for water splitting as a bi-functional electrocatalyst, which can be simultaneously employed to assemble a two-electrode configuration. As

shown in Fig. 4e, it can reach a current density of 10 mA cm$^{-2}$ at a cell voltage of 1.71 V by applying the Co$^{II}$Fe-ONC as both cathode and anode electrodes, which is smaller than that of CoFe-ONC (1.885 V). The stability for the overall water splitting was tested by the chronoamperometry at a cell voltage of 1.81 V (without *iR* compensation) for 15 h (as shown in Fig. 4f). Small changes in current density and overpotential (inside of the Fig. 4f) indicate the excellent stability of the Co$^{II}$Fe-ONC for overall water splitting.

The XPS of Co$^{II}$Fe-ONC after OER and HER test was evaluated to further understand the catalytic performance of Co$^{II}$Fe-ONC. As shown in Fig. 5a, there are red shifts for Co 2p$_{1/2}$ and Co 2p$_{3/2}$ after OER test in accordance with the formation of the Co oxo/hydroxide reported previously [45]. In addition, the Co$^{2+}$/Co$^{3+}$ has dropped from 2.27 to 1.4, indicating that the Co oxy/hydroxide is mainly formed from the Co$^{2+}$ [46–48]. Furthermore, the O 1s spectrum in Fig. 5b illustrates an evident blue shift after the OER test. The peak at 532.2 eV can be associated to the *OOH in the Co oxy/hydroxide [49]. Fig. 5c and d display the Co 2p and O 1s spectra of CoFe-ONC before and after the OER test, which further demonstrate the formation of Co oxy/hydroxide after the OER test from Co$^{2+}$. It can be concluded that a higher Co$^{2+}$/Co$^{3+}$
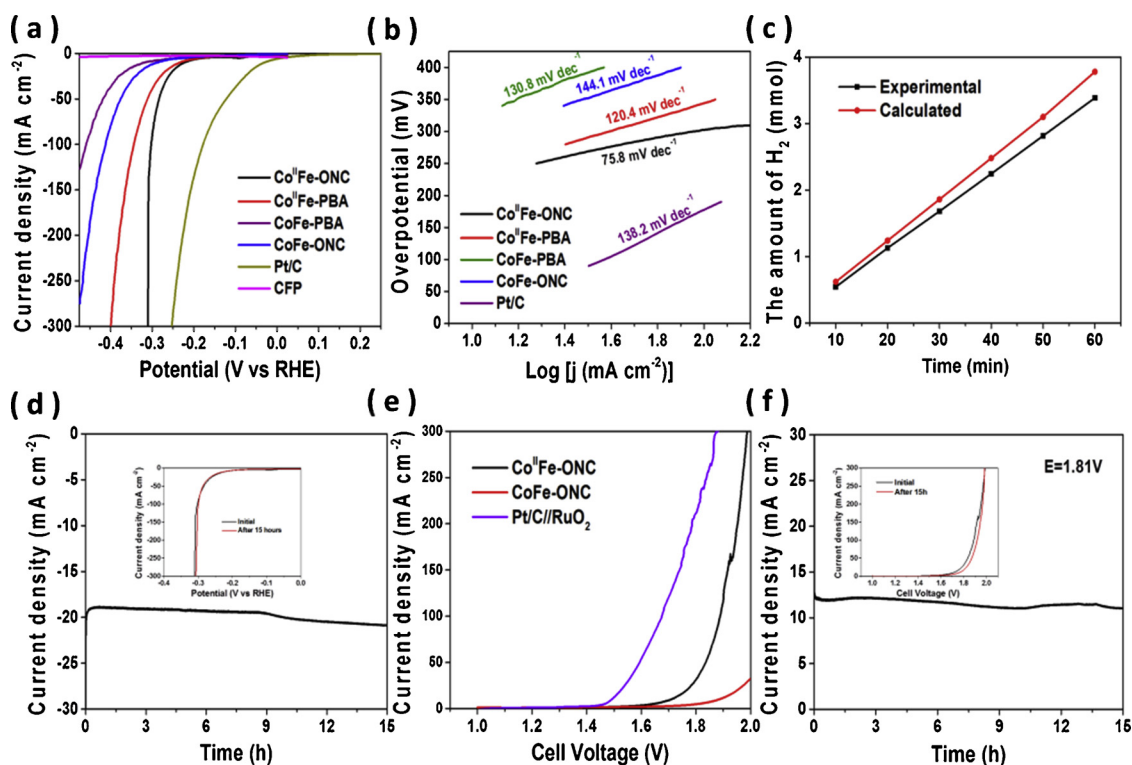
**Fig. 4.** (a) HER LSV curves with 95% *iR* compensation of the as-prepared catalysts, CFP and commercial Pt/C. (b) The corresponding Tafel plots. (c) HER Faradaic efficiency measurement of Co$^{II}$Fe-ONC with a current density of 100 mA cm$^{-2}$. (d) HER stability test without *iR* compensation of the Co$^{II}$Fe-ONC electrode at an overpotential of 315 mV in 1 M KOH for 15 h. The inset shows the LSV curves with 95% *iR* compensation before and after the long-term test. (e) Overall water splitting LSV curves with a 95% *iR* compensation of Co$^{II}$Fe-ONC, CoFe-ONC and Pt/C//RuO$_2$. (f) Long-term stability test of Co$^{II}$Fe-ONC for overall water splitting at 1.81 V without *iR* compensation. The inset shows the LSV curves with 95% *iR* compensation of Co$^{II}$Fe-ONC before and after the long-term test.

might facilitate the formation of Co oxy/hydroxide, which is important for OER. Furthermore, there is no evident change for Co 2p during HER test (Fig. S19), while the peak assigned to *OH in the Co hydroxide can be deconvoluted in O 1s spectrum [50].
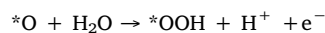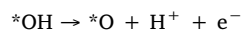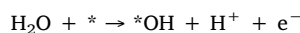
## 3. Discussion

A series of controlled experiments are replenished to clarify our work. Aside from the Co$^{2+}$ reactive sites being optimized by chemical tailoring, the presence of Fe may also be relate to the outstanding electrocatalytic performance. The pristine cobalt oxide (Co$^{II}$Co-ONC, Fig. S20 and S21) derived from Co$^{II}$Co-PBA were prepared by the similar chemical tailoring treatment. A great improvement of both OER and HER performance was observed by introducing Fe (Fig. S22). The Fe dopant preferably enters into the tetrahedral site of the reverse spinel structure to adjust the electronic structure of Co, which causes a higher Co$^{2+}$/Co$^{3+}$ in the Co$^{II}$Fe-ONC and more O-vacancies (Fig. S23) [51]. The electrons occupied oxygen 2p orbitals will delocalize to be neighboring the active sites of Co when the oxygen atom is removed [52]. For one thing, the low-coordinated Co center is highly active to the adsorption of H$_2$O [25,36,53–55]. For another, those delocalized electrons derived from the o-vacancy are easily excited to the conduction band for improved conductivity and OER performance of Co$^{II}$Fe-ONC. Correspondingly, EIS was employed to assess the charge transfer resistance of Co$^{II}$Fe-ONC compared with that of Co$^{II}$Co-ONC. Fig. S24 shows that Co$^{II}$Fe-ONC (1.585 V, R$_{ct}$ = 1.15Ω) has a smaller charge transfer resistance compared with Co$^{II}$Co-ONC (1.585 V, R$_{ct}$ = 4.69Ω), suggesting a more convenient electronic transmission on Fe sites [56,57].

To further understand the nature of valence configuration, both the OER and HER performance of different CoFe oxides with tunable Co$^{2+}$/Co$^{3+}$ ratios by varying the chemical tailoring temperature were

conducted. As shown in Fig. S25, Co$^{II}$Fe-ONC (chemical tailoring at 180°C) exhibits a much better activity than those with smaller Co$^{2+}$/Co$^{3+}$ ratio. Here three models of Co$_3$O$_4$ (111), (Co$^{II}$Fe$^{II}$)(Co$^{III}$Fe$^{III}$)O$_4$ (111), Co$^{II}$(Fe$^{III}$Co$^{III}$)O$_4$ (111) (as shown in the Fig. S26 were established to study the advantage of optimum valence configuration during the water splitting. The detailed computational method is demonstrated in Supplementary Material.

Firstly, H$_2$O adsorption energy of the three models were investigated, as shown in Fig. 6a, the adsorption energy of H$_2$O on the Co$_3$O$_4$ (111), (Co$^{II}$Fe$^{II}$)(Co$^{III}$Fe$^{III}$)O$_4$ (111), Co$^{II}$(Fe$^{III}$Co$^{III}$)O$_4$ (111) are −0.48 eV, −0.52 eV and −0.76 eV, respectively. The higher adsorption energy of Co$^{II}$(Fe$^{III}$Co$^{III}$)O$_4$ (111) indicates a stronger water adsorption capacity for facilitating water splitting. To further understand the electronic nature of the interaction between H$_2$O and the catalysts, the 2D and 3D charge density difference analyses were performed. As H$_2$O being adsorbed on the surface of Co$_3$O$_4$, (Co$^{II}$Fe$^{II}$)(Co$^{III}$Fe$^{III}$)O$_4$ and Co$^{II}$(Fe$^{III}$Co$^{III}$)O$_4$, the electrons transfers from Co atom to O atom as shown in Fig. S27. The strong charge accumulations between Co of Co$^{II}$(Fe$^{III}$Co$^{III}$)O$_4$ (111) and O of H$_2$O further prove the strong water adsorption capacity of the Co$^{II}$(Fe$^{III}$Co$^{III}$)O$_4$ (111).

Furthermore, the reaction free energies on the three models during OER were investigated based on DFT calculation. The process of the OER was considered as the four steps:

$$H_2O + * \rightarrow *OH + H^+ + e^-$$
$$*OH \rightarrow *O + H^+ + e^-$$
$$*O + H_2O \rightarrow *OOH + H^+ + e^-$$
$$*OOH \rightarrow O_2 + * + H^+ + e^-$$

where * denotes the adsorption site of the catalysts, and *OH, *O, *OOH are the intermediate products in OER. The free energy diagrams
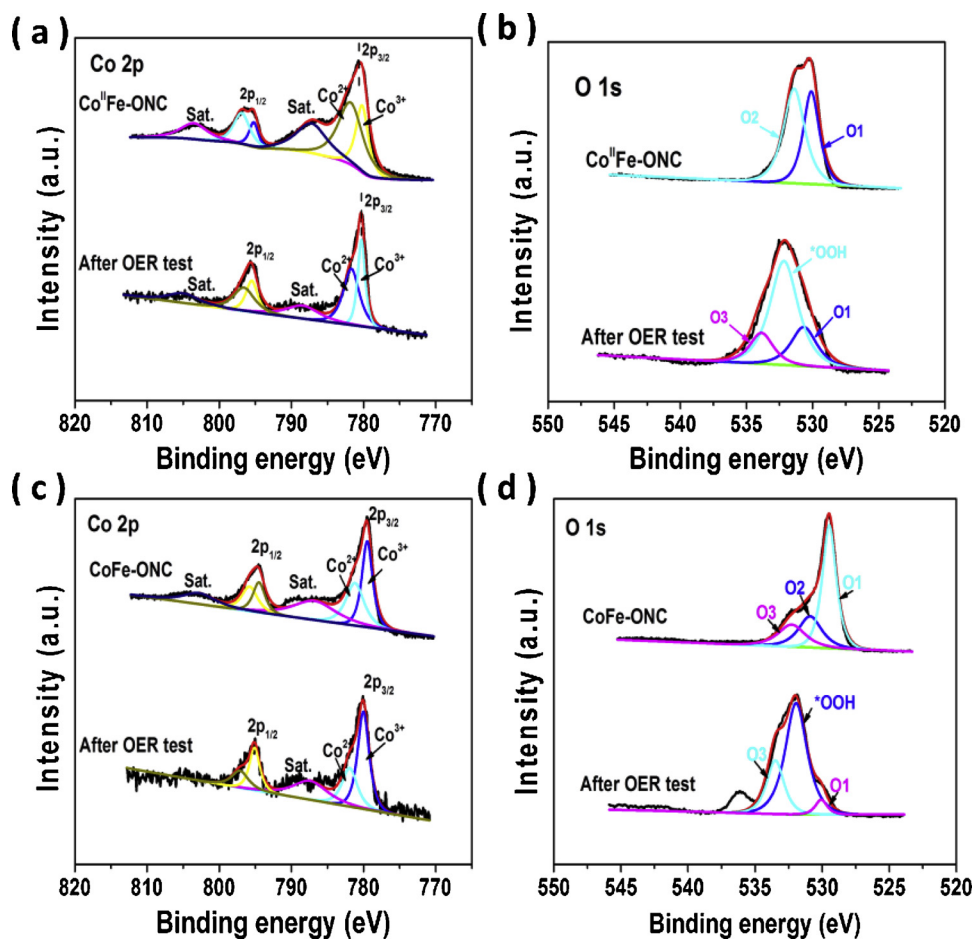
**Fig. 5.** XPS analysis of (a) Co 2p and (b) O 1s in Co$^{II}$Fe-ONC before and after OER test. XPS analysis of (c) Co 2p and (d) O 1s in CoFe-ONC before and after OER test.

on the Co-site of the three models are shown in the Fig. 6b, and the corresponding adsorption configurations of the intermediate products on the Co-site are presented in Fig. S28. It can be easily found that the rate-determining step of Co$_3$O$_4$ and (Co$^{II}$Fe$^{II}$)(Co$^{III}$Fe$^{III}$)O$_4$ is the final release of O$_2$ with an overpotential of 1.63 V and 1.13 V, respectively. However, the rate-determining step on Co$^{II}$(Fe$^{III}$Co$^{III}$)O$_4$ is the formation of *OOH with an overpotential of 0.48 V, indicating that a high Co$^{2+}$/Co$^{3+}$ could reduce the energy barrier of the release of O$_2$. It can be concluded a significant enhancement of OER with Fe presence and high Co$^{2+}$/Co$^{3+}$ ratio, which is in accordance with the experimental results. Here Fe sites in both (Co$^{II}$Fe$^{II}$)(Co$^{III}$Fe$^{III}$)O$_4$ and Co$^{II}$(Fe$^{III}$Co$^{III}$)O$_4$ were evaluated for OER as well (Fig. S29 and S30). The different rate-

determining step and high overpotential reveals that Co dominates the OER active sites and the lower valence state of Co$^{2+}$ prefer higher activity.

Qualitatively, the HER pathway in alkaline media can be described as two steps of (1) electrocouple water dissociation (Volmer step) and (2) subsequent combination of the formed H* into molecular H$_2$, whereas OH$^-$ is released to the solution [58,59]. For various inorganic HER electrocatalysts, the energy of the intermediates has been considered as an important descriptor for assessing the HER activity [60,61]. According to our results, the optimum small value of the absorbed hydrogen (*H) benefits a fast formation of absorbed hydrogen and a rapid concomitant hydrogen release. However, the energy
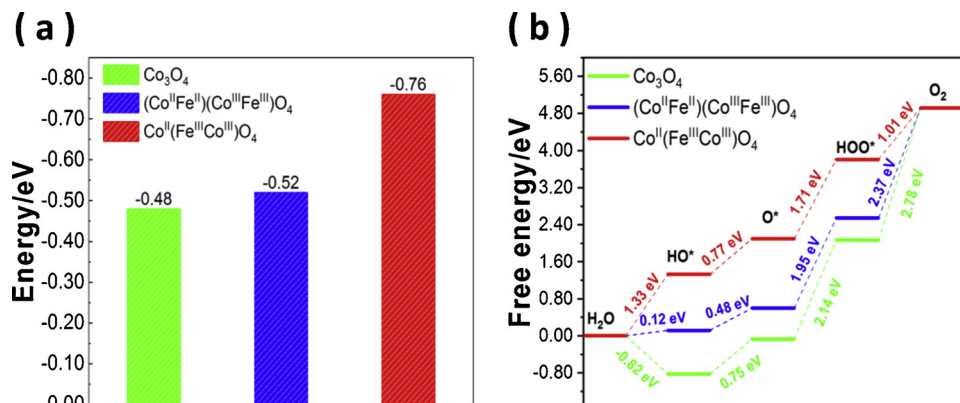


**Fig. 6.** (a) The adsorption energy of H$_2$O for the Co$_3$O$_4$ (111), (Co$^{II}$Fe$^{II}$)(Co$^{III}$Fe$^{III}$)O$_4$ (111), Co$^{II}$(Fe$^{III}$Co$^{III}$)O$_4$ (111). (b) The reaction free energy at the Co-site of the Co$_3$O$_4$ (111), (Co$^{II}$Fe$^{II}$)(Co$^{III}$Fe$^{III}$)O$_4$ (111), Co$^{II}$(Fe$^{III}$Co$^{III}$)O$_4$ (111) for OER.

barriers of the rate-determining step of water dissociation are distinctive for $Co_3O_4$, $(Co^{II}Fe^{II})(Co^{III}Fe^{III})O_4$ and $Co^{II}(Fe^{III}Co^{III})O_4$. Remarkably, the energy barrier for $Co^{II}(Fe^{III}Co^{III})O_4$ (1.0 eV) is substantially lower than that for $Co_3O_4$ (1.64 eV) and $(Co^{II}Fe^{II})(Co^{III}Fe^{III})O_4$ (1.2 eV), presenting a favorable pathway for the dissociation of water. Overall, the theoretical results accord well with the experiment results for both OER and HER in alkali, revealing that valence configuration offers opportunities to create superior electrocatalysts for overall water splitting.

## 4. Conclusions

In summary, we have successfully synthesized the CoFe-oxide nanocubes with a favorable valence configuration of rich $Co^{2+}$ through a chemical tailoring method from CoFe-PBA. The as-synthesized $Co^{II}Fe$-ONC electrocatalysts show excellent activity for overall water splitting, mainly attributed to the introduction of Fe and rich $Co^{2+}$ state in priority. Remarkably, DFT calculation reveals that the lower valence state of Co in $Co^{II}Fe$-ONC efficiently tunes the adsorbing capacity of $H_2O$ and the intermediate products, and optimizing the reaction energy barriers. The as-synthesized $Co^{II}Fe$-ONC electrocatalysts only require small overpotentials of 289 and 284 mV for OER and HER, respectively, at a current density of 50 mA cm$^{-2}$ in 1 M KOH solution. We provided an example that the valence configuration of the active sites should be focused on. This suggests a design strategy beyond traditional nanocatalysts design involving nanostructure, support effect, and defects *etc.*

## Declaration of Competing Interest

The authors declare that they have no known competing financial interests or personal relationships that could have appeared to influence the work reported in this paper.

## Acknowledgements

## Appendix A. Supplementary data

Supplementary material related to this article can be found, in the online version, at doi:https://doi.org/10.1016/j.apcatb.2019.117968.

## References

[1] Y. Zeng, G.-F. Chen, Z. Jiang, L.-X. Ding, S. Wang, H. Wang, J. Mater. Chem. A 6 (2018) 15942–15946.
[2] K. Jayaramulu, J. Masa, O. Tomanec, D. Peeters, V. Ranc, A. Schneemann, R. Zboril, W. Schuhmann, R.A. Fischer, Adv. Funct. Mater. 27 (2017) 1700451.
[3] T. Liu, L. Xie, J. Yang, R. Kong, G. Du, A.M. Asiri, X. Sun, L. Chen, Chemelectrochem 4 (2017) 1840–1845.
[4] T. Zhang, M.Y. Wu, D.Y. Yan, J. Mao, H. Liu, W.B. Hu, X.W. Du, T. Ling, S.Z. Qiao, Nano Energy 43 (2018) 103–109.
[5] T.Y. Ma, J.L. Cao, M. Jaroniec, S.Z. Qiao, Angew. Chem. Int. Ed. 55 (2016) 1138–1142.
[6] L. Xie, C. Tang, K. Wang, G. Du, A.M. Asiri, X. Sun, Small 13 (2017) 1602755.
[7] Z.Q. Wang, X. Ren, L. Wang, G.W. Cui, H.J. Wang, X.P. Sun, Chem. Commun. 54 (2018) 10993–10996.
[8] X. Zhang, Q. Liu, X. Shi, A.M. Asiri, X. Sun, Inorg. Chem. Front. 5 (2018) 1405–1408.
[9] P. Li, R. Zhao, H. Chen, H. Wang, P. Wei, H. Huang, Q. Liu, T. Li, X. Shi, Y. Zhang, M. Liu, X. Sun, Small 15 (2019) 1805103.
[10] J. Suntivich, K.J. May, H.A. Gasteiger, J.B. Goodenough, Y. Shao-Horn, Science 334 (2011) 1383–1385.
[11] B. Zhang, X. Zheng, O. Voznyy, R. Comin, M. Bajdich, M. García-Melchor, L. Han, J. Xu, M. Liu, L. Zheng, Science 352 (2016) 333–337.
[12] D. Chen, C. Chen, Z.M. Baiyee, Z. Shao, F. Ciucci, Chem. Rev. 115 (2015) 9869–9921.
[13] R. Subbaraman, D. Tripkovic, K.-C. Chang, D. Strmcnik, A.P. Paulikas, P. Hirunsit, M. Chan, J. Greeley, V. Stamenkovic, N.M. Markovic, Nat. Mater. 11 (2012) 550–557.
[14] G. Li, X. Wang, J. Fu, J. Li, M.G. Park, Y. Zhang, G. Lui, Z. Chen, Angew. Chem. Int. Ed. 55 (2016) 4977–4982.
[15] J. Wang, Z. Wu, L. Han, R. Lin, H.L. Xin, D. Wang, ChemCatChem 8 (2016) 736–742.
[16] Z.Q. Liu, H. Cheng, N. Li, T.Y. Ma, Y.Z. Su, Adv. Mater. 28 (2016) 3777–3784.
[17] Z. Wang, H. Liu, R. Ge, X. Ren, J. Ren, D. Yang, L. Zhang, X. Sun, ACS Catal. 8 (2018) 2236–2241.
[18] X.P. Han, G.W. He, Y. He, J.F. Zhang, X.R. Zheng, L.L. Li, C. Zhong, W.B. Hu, Y.D. Deng, T.Y. Ma, Adv. Energy Mater. 8 (2018) 1702222.
[19] L. Han, X.Y. Yu, X.W. Lou, Adv. Mater. 28 (2016) 4601–4605.
[20] Y.P. Zhu, T.Y. Ma, M. Jaroniec, S.Z. Qiao, Angew. Chem. Int. Ed. 56 (2017) 1324–1328.
[21] W. Liu, H. Liu, L. Dang, H. Zhang, X. Wu, B. Yang, Z. Li, X. Zhang, L. Lei, S. Jin, Adv. Funct. Mater. 27 (2017) 1603904.
[22] J. Wang, F. Ciucci, Small 13 (2017) 1604103.
[23] H. Hu, B. Guan, B. Xia, X.W. Lou, J. Am. Chem. Soc. 137 (2015) 5590–5595.
[24] Y. Sun, T. Zhang, X. Li, D. Liu, G. Liu, X. Zhang, X. Lyu, W. Cai, Y. Li, Chem. Commun. 53 (2017) 13237–13240.
[25] Y. Wang, T. Zhou, K. Jiang, P. Da, Z. Peng, J. Tang, B. Kong, W.B. Cai, Z. Yang, G. Zheng, Adv. Energy Mater. 4 (2014) 1400696.
[26] L. Xu, Q. Jiang, Z. Xiao, X. Li, J. Huo, S. Wang, L. Dai, Angew. Chem. Int. Ed. 55 (2016) 5277–5281.
[27] X. Zhang, J. Li, Y. Yang, S. Zhang, H. Zhu, X. Zhu, H. Xing, Y. Zhang, B. Huang, S. Guo, E. Wang, Adv. Mater. 30 (2018) 1803551.
[28] H. Zhang, X. Liu, Y. Wu, C. Guan, A.K. Cheetham, J. Wang, Chem. Commun. 54 (2018) 5268–5288.
[29] A. Kumar, S. Bhattacharyya, ACS Appl. Mater. Interfaces 9 (2017) 41906–41915.
[30] S. Lei, Q.-H. Li, Y. Kang, Z.-G. Gu, J. Zhang, Appl. Catal. B 245 (2019) 1–9.
[31] M. Hu, S. Furukawa, R. Ohtani, H. Sukegawa, Y. Nemoto, J. Reboul, S. Kitagawa, Y. Yamauchi, Angew. Chem. Int. Ed. 51 (2012) 984–988.
[32] P. Cai, J. Huang, J. Chen, Z. Wen, Angew. Chem. Int. Ed. 129 (2017) 4936–4939.
[33] C.-W. Tung, Y.-Y. Hsu, Y.-P. Shen, Y. Zheng, T.-S. Chan, H.-S. Sheu, Y.-C. Cheng, H.M. Chen, Nat. Commun. 6 (2015).
[34] T. Zhai, L. Wan, S. Sun, Q. Chen, J. Sun, Q. Xia, H. Xia, Adv. Mater. 29 (2017) 1604167.
[35] G. Wu, J. Wang, W. Ding, Y. Nie, L. Li, X. Qi, S. Chen, Z. Wei, Angew. Chem. Int. Ed. 55 (2016) 1340–1344.
[36] J. Bao, X. Zhang, B. Fan, J. Zhang, M. Zhou, W. Yang, X. Hu, H. Wang, B. Pan, Y. Xie, Angew. Chem. Int. Ed. 54 (2015) 7399–7404.
[37] Z. Cai, Z. Bi, E. Hu, W. Liu, N. Dwarica, Y. Tian, X. Li, Y. Kuang, Y. Li, X.-Q. Yang, H. Wang, X. Sun, Adv. Energy Mater. 8 (2018) 1701694.
[38] S. Guo, S. Zhang, L. Wu, S. Sun, Angew. Chem. Int. Ed. 124 (2012) 11940–11943.
[39] S. Chen, L. Wang, Q. Wu, X. Li, Y. Zhao, H. Lai, L. Yang, T. Sun, Y. Li, X. Wang, Sci. China Mater. 58 (2015) 180–186.
[40] Q. Fu, W.-X. Li, Y. Yao, H. Liu, H.-Y. Su, D. Ma, X.-K. Gu, L. Chen, Z. Wang, H. Zhang, Science 328 (2010) 1141–1144.
[41] G. Wei, Z. Zhou, X. Zhao, W. Zhang, C. An, ACS Appl. Mater. Interfaces 10 (2018) 23721–23730.
[42] M. Görlin, P. Chernev, J. Ferreira de Araújo, T. Reier, Sr. Dresp, B. Paul, R. Krähnert, H. Dau, P. Strasser, J. Am. Chem. Soc. 138 (2016) 5603–5614.
[43] Y. Chen, J. Zhang, P. Guo, H. Liu, Z. Wang, M. Liu, T. Zhang, S. Wang, Y. Zhou, X. Lu, J. Zhang, ACS Appl. Mater. Interfaces 10 (2018) 27787–27794.
[44] T. Wang, D. Gao, W. Xiao, P. Xi, D. Xue, J. Wang, Nano Res. 11 (2018) 6051–6061.
[45] S. Jin, ACS Energy Lett. 2 (2017) 1937–1938.
[46] C.-S. Hsu, N.-T. Suen, Y.-Y. Hsu, H.-Y. Lin, C.-W. Tung, Y.-F. Liao, T.-S. Chan, H.-S. Sheu, S.-Y. Chen, H.M. Chen, Phys. Chem. Chem. Phys. 19 (2017) 8681–8693.
[47] M.E.G. Lyons, M.P. Brandon, J. Electrochem. Soc. 631 (2009) 62–70.
[48] H.-Y. Wang, S.-F. Hung, H.-Y. Chen, T.-S. Chan, H.M. Chen, B. Liu, J. Am. Chem. Soc. 138 (2015) 36–39.
[49] S. Li, S. Sirisomboonchai, A. Yoshida, X. An, X. Hao, A. Abudula, G. Guan, J. Mater. Chem. A 6 (2018) 19221–19230.
[50] B. Hua, M. Li, Y.-F. Sun, Y.-Q. Zhang, N. Yan, J. Chen, T. Thundat, J. Li, J.-L. Luo, Nano Energy 32 (2017) 247–254.
[51] Y. Liu, Y. Ying, L. Fei, Y. Liu, Q. Hu, G. Zhang, S.Y. Pang, W. Lu, C.L. Mak, X. Luo, L. Zhou, M. Wei, H. Huang, J. Am. Chem. Soc. 141 (2019) 8136–8145.
[52] L. Zhuang, Y. Jia, T. He, A. Du, X. Yan, L. Ge, Z. Zhu, X. Yao, Nano Res. (2018) 1–10.
[53] L. Zhuang, L. Ge, Y. Yang, M. Li, Y. Jia, X. Yao, Z. Zhu, Adv. Mater. 29 (2017) 1606793.
[54] R.G. Hadt, D. Hayes, C.N. Brodsky, A.M. Ullman, D.M. Casa, M.H. Upton, D.G. Nocera, L.X. Chen, J. Am. Chem. Soc. 138 (2016) 11017–11030.
[55] J. Wang, X. Ge, Z. Liu, L. Thia, Y. Yan, W. Xiao, X. Wang, J. Am. Chem. Soc. 139 (2017) 1878–1884.
[56] L. Trotochaud, S.L. Young, J.K. Ranney, S.W. Boettcher, J. Am. Chem. Soc. 136 (2014) 6744–6753.
[57] D.A. Corrigan, J. Electrochem. Soc. 134 (1987) 377–384.
[58] M. Gong, D.-Y. Wang, C.-C. Chen, B.-J. Hwang, H. Dai, Nano Res. 9 (2016) 28–46.
[59] X. Chen, K. Xu, S. Tao, Y. Zhou, Y. Tong, H. Ding, L. Zhang, W. Chu, C. Wu, Y. Xie, Adv. Mater. 28 (2016) 7527–7532.
[60] Y. Zheng, Y. Jiao, Y. Zhu, L.H. Li, Y. Han, Y. Chen, A. Du, M. Jaroniec, S.Z. Qiao, Nat. Commun. 5 (2014) 3783.
[61] Y. Zheng, Y. Jiao, L.H. Li, T. Xing, Y. Chen, M. Jaroniec, S.Z. Qiao, ACS Nano 8 (2014) 5290–5296.